

# PIC Simulation Study of Merging Processes of Two Spheromak-Like Plasmoids<sup>\*)</sup>

Ritoku HORIUCHI, Toseo MORITAKA and Shunsuke USAMI

*National Institute for Fusion Science, Toki 509-5292, Japan*

(Received 25 December 2017 / Accepted 25 March 2018)

Two different types of merging processes of spheromak-like plasmoids (SPs) without any external guide-field (toroidal) component, which are confined in a rectangular conducting vessel, have been investigated by means of two-dimensional PIC simulation, i.e., counter-helicity merging and co-helicity merging processes. The merging time scale is given by the transit time for ion sound wave to travel from the center of SP in the initial profile to the reconnection point for both cases. Through the counter-helicity SP merging process, toroidal magnetic field energy is effectively converted to thermal energy, while the energy transfer rate is suppressed to lower value for the co-helicity case because most of the toroidal magnetic field energy does not dissipate in the merging process. The reconnection process is impulsive for both cases, and, thus, the released energy is locally distributed around field lines connected to a reconnection point and forms the high temperature region with a spatial structure dependent on Larmor radius and the merging processes.

© 2018 The Japan Society of Plasma Science and Nuclear Fusion Research

Keywords: spheromak, counter-helicity merging, co-helicity merging, PIC simulation, magnetic reconnection, energy transfer

DOI: 10.1585/pfr.13.3403035

## 1. Introduction

Physics of magnetic reconnection have been studied typically through two approaches. One is an experimental study using merging processes of two spheromak plasmas [1] or spherical tokamak plasmas [2]. The other is a particle-in-cell (PIC) simulation study in an open system [3, 4], which mimics the vicinity of the reconnection point in the merging process. Two approaches have so far clarified common pictures of magnetic reconnection [1–4]. However, because these studies have been carried out based on different configurations, we should be careful in comparing the results of the two approaches. For example, in contrast to collisionless reconnection in an open system [3, 4], most of the plasma and energy are confined inside a newly formed plasmoid after the merging in the experiments. Furthermore, because the magnetic energy available for the merging process is limited, reconnection itself is time-dependent and becomes impulsive in some cases. On the other hand, we can realize constant reconnection phenomena in an open system by supplying the energy from the outside of a system constantly. These characteristics in the merging processes reveal new features of magnetic reconnection different from those in an open system.

In this paper we have extended our PIC simulation model and applied it to the two different types of merging processes of two spheromak-like plasmoids (SPs),

which are confined in a conducting rectangular vessel, i.e., counter-helicity merging and co-helicity merging processes.

## 2. Simulation Model

Our PIC simulation model is implemented on two-dimensional Cartesian coordinates  $(x, y)$ . The perfect conductor wall is located at the boundaries of the  $x$ -axis ( $x = \pm 128dx$ ), and the periodic condition is adopted at the boundaries of the  $y$ -axis ( $y = \pm 512dy$ ), where  $dx$  and  $dy$  ( $= dx$ ) are the grid separations along the  $x$ -axis and  $y$ -axis, respectively. Two SPs, which satisfy an MHD equilibrium condition, are located along the  $y$ -axis inside a conducting rectangular vessel at initial stage. After solving the Grad-Shafranov equation in terms of the poloidal flux function  $\Psi(x, y)$ , initial magnetic field  $\mathbf{B}(x, y)$  and thermal pressure  $P(x, y)$  are given by the following equations as

$$\mathbf{B} = (\partial\Psi/\partial y, -\partial\Psi/\partial x, B_z), \quad (1)$$

$$B_z = B_p\phi^\alpha, \quad p = p_{ax}\phi^\epsilon, \quad (2)$$

where  $\phi(x, y) = (\Psi - \Psi_{lim})/(\Psi_{ax} - \Psi_{lim})$ , and  $\alpha$  ( $= 1.6$ ),  $\epsilon$  ( $= 1.2$ ),  $\Psi_{ax}$ ,  $\Psi_{lim}$ , and  $p_{ax}$  are constant parameters. The parameter  $p_{ax}$  is determined so that the average plasma beta is equal to  $\beta = 0.2$ . Figure 1 plots the spatial profiles of magnetic fields, thermal pressure, and electron Larmor radius along the line connecting the centers of two SPs for the co-helicity (solid) and counter-helicity (dashed) merging cases. The poloidal current density ( $J_x, J_y$ ) and toroidal magnetic field  $B_z$  in one SP have an opposite sign to those in the other SP for the counter-helicity case. The ini-

author's e-mail: horiuchi.ritoku@toki-fs.jp

<sup>\*)</sup> This article is based on the presentation at the 26th International Toki Conference (ITC26).

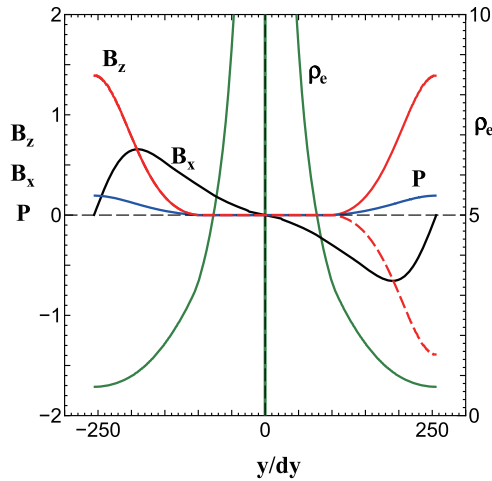


Fig. 1 MHD equilibrium solution for the co-helicity (solid) and counter-helicity (dashed) merging processes. The spatial profiles of magnetic field ( $B_x, B_z$ ), thermal pressure ( $P$ ), and electron Larmor radius ( $\rho_e$ ) are plotted along the line connecting the centers of the two SPs.

tial conditions for the PIC simulation are obtained from the MHD equilibrium solution by assuming that electric current density consists of the force-free and diamagnetic components, the force-free component is carried only by electrons, and particle temperature and number density satisfy the following relations as

$$T_e = T_i = \text{constant}, \quad n_e = n_i. \quad (3)$$

The number of space grids is  $(256 \times 1024)$ , and the total number of particles is 0.2 billion, including the uniform background particles of 20 per each space cell. The aspect ratio of the simulation box is  $Y_{\text{eng}}/X_{\text{eng}} = 4.0$ . We have carried out eleven simulation runs for different mass ratio  $M_i/M_e$  ( $= 100, 200, 400, 800$ ) and two types of the combination of magnetic helicity to clarify the roles of ion and electron dynamics for the co-helicity and counter-helicity cases. That is, two series of simulation runs were carried out to clarify the roles of (1) the electron dynamics and (2) the ion dynamics for the counter-helicity merging. On the other hands, a series of the simulation runs were carried out to clarify the role of the ion dynamics for the co-helicity merging. For example, when the electron dynamics is examined, the electron parameters vary according to the mass ratio while keeping the ion parameters such as the ion Larmor radius constant.

### 3. Counter-Helicity Merging

It is well-known from the experimental studies [1] that the field-reversed configuration (FRC) is formed as a result of counter-helicity merging of two spheromaks which have the magnetic helicity of the same amplitude but opposite sign. First, let us examine the relaxation process of two SPs to one FRC-like plasmoid by using the PIC simulation. Figure 2 demonstrates the time evolution of the mag-

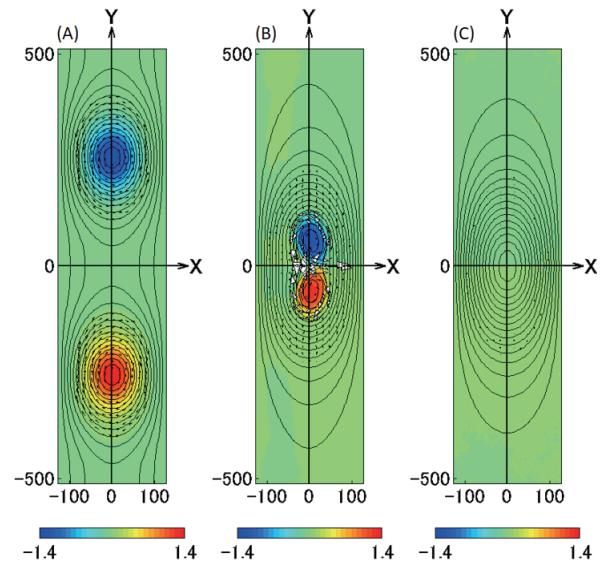


Fig. 2 Time evolution of magnetic field and poloidal electron flow velocity for the counter-helicity merging case of  $M_i/M_e = 400$ , where the color contours, lines, and arrows stand for toroidal magnetic field  $B_z$ , poloidal magnetic field lines, and electron flow velocity in  $(x, y)$  plane, respectively. The  $x$ - and  $y$ -coordinates are normalized by the grid separations  $dx$  and  $dy$  along the  $x$ -axis and  $y$ -axis, respectively. Time evolves from the left to the right, i.e., (A)  $\omega_{pi}t = 0$ , (B)  $\omega_{pi}t = 230$ , and (C)  $\omega_{pi}t = 920$ .

netic field and the poloidal electron flow velocity ( $v_x, v_y$ ) for the counter-helicity merging case of  $M_i/M_e = 400$ . Two SPs have the opposite electron rotation in poloidal plane, sustaining toroidal magnetic fields with the opposite sign. Magnetic reconnection takes place at the interface region, where electrons flow in the positive  $x$ -direction. Because most of the electrons are magnetized and their motion drags magnetic field lines as soon as they leave the reconnection region, a reconnection point moves towards the positive  $x$ -direction. The  $x$ -axis corresponds to the radial direction in the toroidal system, and the motion of the reconnection point agrees with the counter-helicity experiment in MRX [5] and the Hall-MHD simulation study [6]. Both the toroidal magnetic field and the poloidal current density disappear and only the toroidal current sustaining the poloidal magnetic field exists after the merging. In this way, the FRC-like plasmoid is generated as a result of the counter-helicity merging of two SPs.

Figure 3 shows the time evolution of integrated energies for the same case with Fig. 2, where the red, blue, green, black, orange, black dashed curves stand for the magnetic field energy ( $W_{\text{mag}}$ ), the electric field energy ( $W_{\text{efd}}$ ), the ion kinetic energy ( $W_{\text{ki}}$ ), the ion thermal energy ( $W_{\text{ti}}$ ), the electron kinetic energy ( $W_{\text{ke}}$ ), the electron thermal energy ( $W_{\text{te}}$ ), respectively. The energy is averaged over the confinement region surrounded by the closed field line, but not over the whole simulation domain. Because a part of the energy leaks outside the confinement region

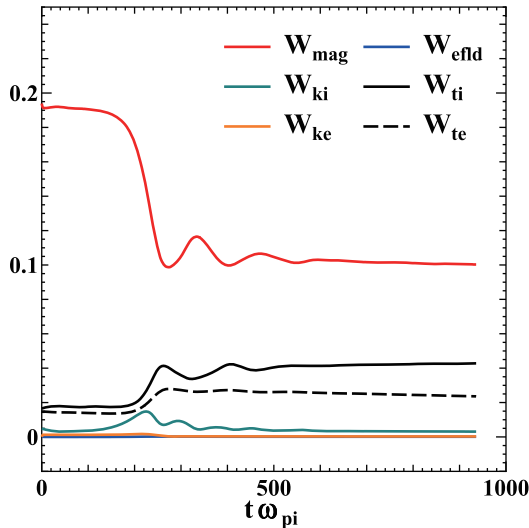


Fig. 3 Time evolution of integrated energies for the counter-helicity merging case of  $M_i/M_e = 400$ . The energy is averaged over the confinement region, and expressed in an arbitrary unit.

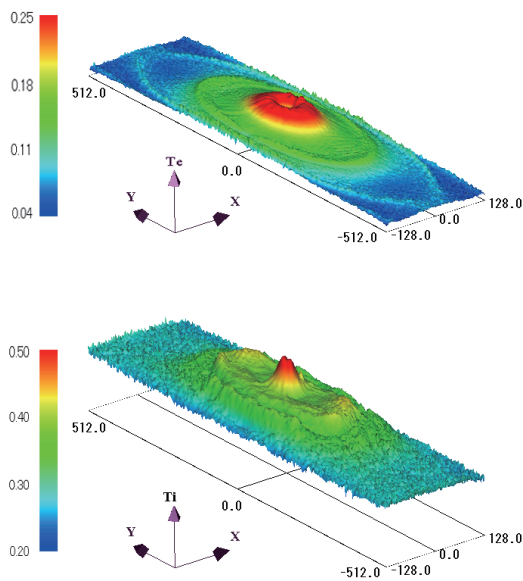


Fig. 4 Perspective view of electron (top) and ion (bottom) temperature profiles in the  $(x, y)$ -plane at  $\omega_{pi}t = 920$  for the counter-helicity merging case of  $M_i/M_e = 400$ , where a height and a color stand for the particle temperature.

through the merging process, the total energy integrated over the confinement region is not conserved at the merging. Through the counter-helicity SP merging process, toroidal magnetic field energy is effectively converted to particle thermal energy. In particular, ion thermal energy becomes twice as much as electron thermal energy. It is also found that the relaxation time scale is almost independent of the electron mass for the counter-helicity merging cases. Figure 4 demonstrates the perspective view of electron (top) and ion (bottom) temperature profiles in the

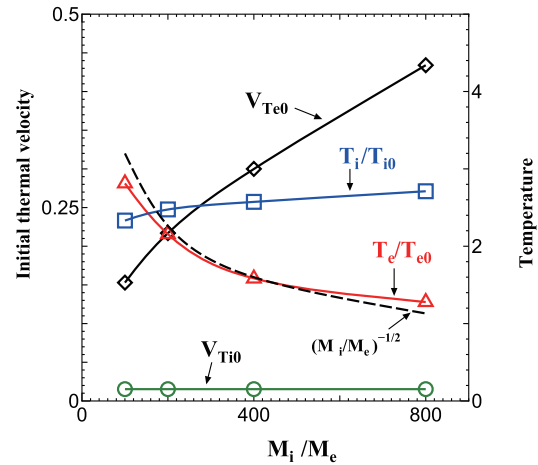


Fig. 5 Electron-mass dependence of the average electron (red) and ion (blue) temperatures after the counter-helicity merging, where the initial electron and ion thermal velocities are also plotted by black and green curves.

$(x, y)$ -plane at  $\omega_{pi}t = 920$  for the same case with Fig. 2, where the particle temperature is defined by the average of the diagonal components of the pressure tensor divided by  $n_{i/e}M_e c^2$ . The ion temperature profile is peaked at the center, while a ring-shaped structure appears around the center in the electron temperature profile. Because the reconnection process is impulsive as seen in Fig. 3, the released energy is locally distributed around a field line connected to a reconnection point when the reconnection rate becomes maximum. As soon as the electrons leave the reconnection region, they are magnetized and move along the field lines. Thus, high-temperature electrons distribute in a ring-shaped region formed around the center of the merged plasmoid. On the other hand, since the field-null region exists near the center and most of the ions are not magnetized there, the ions heated in the reconnection region can easily move into the field-null region and form a peaked temperature profile at the center. It is well-known that high-temperature ions in the field-null region execute a betatron motion and play an important role in stabilizing the tilting instability as one of the most dangerous MHD instabilities in the FRC plasma [7, 8]. It is interesting to note in Fig. 4 that high-temperature ions exist also outside the confinement region, while the electron temperature is very low there. This is because the ion frozen-in condition is violated in a relatively wider region around the reconnection point compared with the electrons, and the ions heated through magnetic reconnection easily move outside the confinement region. The electron-mass dependence of the average electron and ion temperatures after the counter-helicity merging is plotted in Fig. 5, where the particle temperature is averaged over the confinement region and normalized by its initial value. The average electron temperature decreases in proportion to  $(M_i/M_e)^{-1/2}$  as the electron mass decreases. This result may be ex-

plained from the fact that the size of the electron dissipation region is determined by the product of the electron meandering orbit size in the  $x$ -direction and that in the  $y$ -direction, which is in proportion to  $M_e^{1/2}$  [9]. On the other hands, the average ion temperature is almost constant, and becomes lower than the average electron temperature for  $M_i/M_e = 100$ . This phenomenon may be explained from the fact that, as was shown in Fig. 4, the high-temperature ions are also distributed outside the confinement region as well as inside the confinement region, while most of the high-temperature electrons exist inside the confinement region.

### 4. Co-Helicity Merging

Figure 6 demonstrates the time evolution of magnetic field (color contours, lines) and poloidal electron flow velocity (arrows) for the co-helicity merging case of  $M_i/M_e = 400$ . Two SPs have the same plasma rotation in the poloidal plane, sustaining toroidal magnetic field  $B_z$  with the same sign. Magnetic reconnection takes place at the center of the interface region in contrast to counter-helicity merging. As reconnection proceeds, the toroidal magnetic field penetrates into the reconnection region, which tends to suppress reconnection itself. Thus, only a part of the poloidal magnetic field energy is converted to the particle energy. One large SP is generated as a result of the co-helicity merging of two SPs.

Let us compare the merging processes for the co-helicity and counter-helicity cases. Figure 7 plots the ion-mass dependence of the merging time scale for co-helicity (red) and counter-helicity (brown) cases, where the merging time is defined by the time when the total magnetic energy dissipates and reaches the middle value between the initial and the final values. The merging time scale strongly depends on the ion mass for both cases, although it is almost independent of the electron mass. It is worthy of notice that the merging time is nearly equal to the transit time for the ion sound wave to travel from the center of the SP in the initial profile to the reconnection point. Figure 8 shows the ion-mass dependence of the average elec-

ing time is defined by the time when the total magnetic energy dissipates and reaches the middle value between the initial and the final values. The merging time scale strongly depends on the ion mass for both cases, although it is almost independent of the electron mass. It is worthy of notice that the merging time is nearly equal to the transit time for the ion sound wave to travel from the center of the SP in the initial profile to the reconnection point. Figure 8 shows the ion-mass dependence of the average elec-

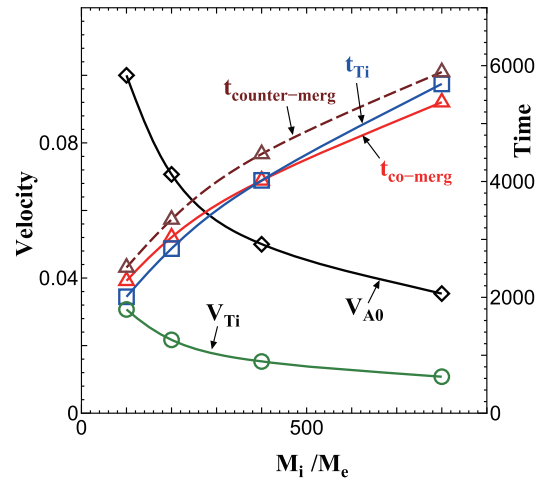


Fig. 7 Ion-mass dependence of the merging time scale for co-helicity (red) and counter-helicity (brown) cases, where the transit time for ion sound wave to travel from the center of SP in the initial profile to the reconnection point is also plotted by a blue line.

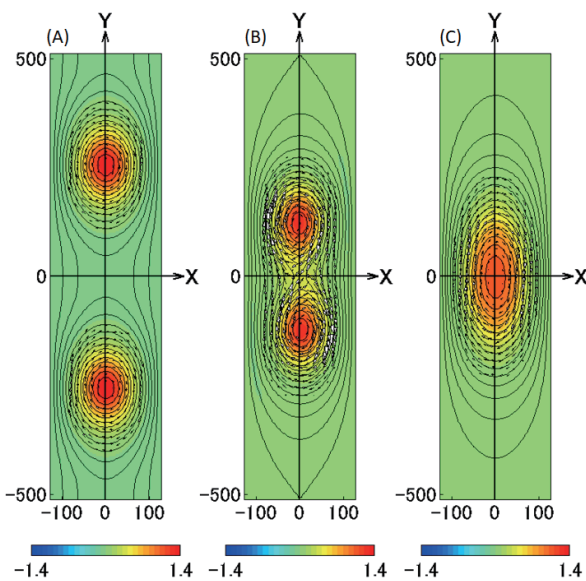


Fig. 6 Time evolution of magnetic field and poloidal electron flow velocity for the co-helicity merging case of  $M_i/M_e = 400$ , where the left, middle, and right panels correspond to the spatial profiles at (A)  $\omega_{pi}t = 0$ , (B)  $\omega_{pi}t = 192$ , and (C)  $\omega_{pi}t = 920$ , respectively.

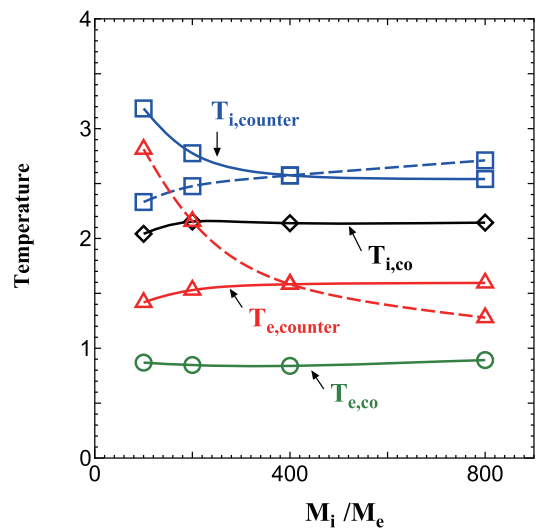


Fig. 8 Ion-mass dependence of the average electron (red and green) and ion (blue and black) temperatures after the co-helicity (black and green) and counter-helicity (blue and red) merging processes. The particle temperature is averaged over the confinement region and normalized by its initial value. The electron-mass dependences of the particle temperatures for the counter-helicity merging are also attached by the dashed curves for comparison.

tron and ion temperatures after the co-helicity and counter-helicity mergings, where the average was taken over the confinement region. Both the ion and the electron temperatures are barely dependent on the ion mass except the small mass ratio case of  $M_i/M_e = 100$ . This result suggests that the dissipation of the electromagnetic energy in the two-dimensional collisionless reconnection takes place dominantly inside the electron dissipation region around the reconnection point, which is controlled by the electron dynamics but not by the ion dynamics [10]. The particle temperatures for the co-helicity case remains at the lower level compared with those for the counter-helicity case. This is because the toroidal component of magnetic field energy hardly dissipates for the co-helicity case, while it dissipates perfectly and is transferred to the particle thermal energy for the counter-helicity case.

## 5. Summary

Two different types of merging processes of spheromak-like (SP) plasmoids, which are confined in a rectangular conducting vessel, have been investigated by means of two-dimensional PIC simulation. Although our simulation model is constructed on the assumptions of no toroidicity and no three-dimensional effects, we have

succeeded in clarifying several fundamental aspects of merging processes of two SPs, i.e., mass-ratio dependence of the merging time scale, energy transfer process, motion of a reconnection point for counter-helicity case, the formation of a ring-shaped electron high-temperature region, and other phenomena.

## Acknowledgments

The simulation was performed by employing the Plasma Simulator at the National Institute for Fusion Science (NIFS). This study was partially supported by General Coordinated Research at the NIFS (NIFS17KNSS097).

- [1] Y. Ono *et al.*, Nucl. Fusion **43**, 649 (2003).
- [2] Y. Ono *et al.*, Phys. Plasmas **4**, 1953 (1997).
- [3] W. Pei *et al.*, Phy. Rev. Lett. **87**, 235003 (2001).
- [4] R. Horiuchi *et al.*, Earth Planets Space **53**, 439 (2001).
- [5] M. Inomoto *et al.*, Phy. Rev. Lett. **97**, 135002 (2006).
- [6] Y. Kaminou *et al.*, Phys. Plasmas **24**, 032508 (2017).
- [7] L.C. Steinhauer, Phys. Plasmas **18**, 070501 (2011).
- [8] R. Horiuchi *et al.*, Phys. Fluids **B2**, 2652 (1990).
- [9] R. Horiuchi *et al.*, Phys. Plasmas **1**, 3587 (1994).
- [10] S. Zenitani *et al.*, Phy. Rev. Lett. **106**, 195003 (2011).